ORIGINAL ARTICLE

Theoretical and experimental investigations of vanadium pentoxide–based electrocatalysts for the hydrogen evolution reaction in alkaline media

Dima Abu Alhawa[1] · Ahmed Badreldin[1] · Abdellatif El-Ghenymy[1] · Noor Hassan[1] · Yiming Wubulikasimu[1] · Khaled Elsaid[1] · Ahmed Abdel-Wahab[1,2,3]

Abstract

A key approach towards better realization of intermittent renewable energy resources, namely, solar and wind, is green electrochemical hydrogen production from water electrolysis. In recent years, there have been increasing efforts aimed at developing noble metal-free electrocatalysts that are earth-abundant and electroactive towards hydrogen evolution reaction (HER) in alkaline electrolytes, wherein an initial water dissociation step is followed by a two-electron transfer cathodic reaction. Although relatively earth-abundant, vanadium-based electrocatalysts have been sparsely reported due to subpar electroactivity and kinetics towards water electrolysis in general and alkaline electrolysis in specific. Herein, we investigate the fine-tuning of orthorhombic V_2O_5-based electrocatalysts as candidates for HER through a scalable two-step sol–gel calcination procedure. Briefly, surface-induced anionic oxygen deficiencies and cationic dopants are synergistically studied experimentally and theoretically. To that end, first-principle facet-dependent density function theory (DFT) calculations were conducted and revealed that the coupling of certain dopants on V_2O_5 and co-induction of oxygen vacancies can enhance the catalytic HER performance by the creation of new electronic states near the Fermi level (E_F), enhancing conductivity, and modulating surface binding of adsorbed protons, respectively. This was reflected experimentally through kinetically non-ideal alkaline electrochemical HER using $Zn_{0.4}V_{1.6}O_5$ whereby -194 mV of overpotential was required to attain -10 mA/cm^2 of current density, as opposed to pristine V_2O_5 which required 32% higher overpotential requirement at the same conditions. The disclosed work can be extended to other intrinsically sluggish transition metal (TM)–based oxides via the presented systematic tuning of surface and bulk microenvironment modulation.

Keywords Hydrogen evolution reaction · Vanadium oxide · V_2O_5 DFT · Oxygen vacancy · Transition metal oxide

✉ Ahmed Badreldin
  ahmed.badreldin@qatar.tamu.edu

✉ Ahmed Abdel-Wahab
  ahmed.wahab@qatar.tamu.edu;
  ahmed.abdel-wahab@qatar.tamu.edu

1 Chemical Engineering Program, Texas A&M University at Qatar, P.O. 23874, Doha, Qatar

2 Department of Materials Science and Engineering, Texas A&M University, College Station, TX 77843, USA

3 Zachry Department of Civil & Environmental Engineering, Texas A&M University, College Station, TX 77843, USA

1 Introduction

Providing clean, affordable energy to the world's expanding population continues to be a major challenge [1]. Although fossil fuels still dominate the world's energy landscape, sustainable energy technologies like wind and solar are becoming increasingly more appealing alternatives due to growing concerns about the impact of anthropogenic carbon dioxide (CO_2) on the planet [2–5]. However, the introduction of these intrinsically intermittent renewable energy sources has been hampered by the difficulties associated with energy storage and integration into existing power systems [6, 7]. It has been debated that the cleanest and most likely contender to replace carbon-based fuels in the foreseeable future is hydrogen (H_2). H_2 has a high calorific value and emits no CO_2 upon combustion [8–10]. From a scalability facet,

QATAR UNIVERSITY   ② Springer

electrochemical water splitting technology combined with grid-scale renewable energy harvesting infrastructures may effectively transform intermittent renewable energy electricity into more value-added H_2, increasing the variety of renewable energy utilization [11]. Currently, fossil fuel processing, including coal gasification, naphtha/oil reforming, and steam methane reforming, produces about 96% of the annual global H_2 supply, whereas around 4% comes from green water electrolysis, resulting in significant emissions of CO_2 and high energy use for the former [12]. In relation to water electrolysis, costly noble metals like Pt, Ru, and Pd make excellent HER electrocatalysts due to near-ideal thermoneutrality towards hydrogen binding [13]. However, their excessive price and limited availability drive significant research towards more cost-effective earth-abundant counterparts without sacrificing on performance [14–17]. Optimization of surface electronics towards reaction intermediates, conductivities, and the electrochemical surface area (ECSA) of TM-based electrocatalysts are essential performance indicators for practical application of emerging electrocatalysts [13, 18–22]. A variety of earth-abundant materials, including carbon-based structures [23, 24], sulfides [25], nitrides [26], carbides [16, 17, 27], and oxides [28–30] have been reported with promising activities.

Whereas conventional HER is typically conducted under acidic conditions, operation in alkaline media promotes the more kinetically sluggish anodic four-electron transfer oxygen evolution reaction (OER). Notwithstanding, operation in alkaline environments results in an initial water dissociation step at the cathode which adds to the cathodic HER overpotential requirements. Diverse tactics were investigated towards enhancing HER activity in non-acidic pH regimes, including inducing surface heterojunctions, elemental doping, and defect engineering, of which oxophilic metal hydroxides on the surface of the cathode has been proposed, which demonstrated optimized HER activity in both alkaline and neutral media, in which the Volmer process is a rate-limiting step, and it holds promise as an attractive method to promote the dissociation of water molecules [31]. Given its affordability and design flexibility, molybdenum sulfide (MoS_2) is among the most popular prospects as an HER electrocatalyst and remains to be among the most studied earth-abundant cathodic materials to date [13, 32]. While different TM-based oxide materials would, in theory, be energetically advantageous for effective HER, a seemingly bottlenecking predicament arises with their electrochemical and chemical stability, which affects their performance in acidic media [33]. To that end, TM-based oxide cathodes such as tungsten trioxide (WO_3) and zinc oxide (ZnO) have been reported to attain poor performance due to unfavorable conductivities, low active site densities, and subpar intermediate energetics. Surface modulation through vacancy induction has, however, been reported to enhance both activity

and stability during HER [19, 34]. Further, through phase-specific heterojunctions with conductive carbon supports, Mineo et al. recently showcased that monoclinic WO_3 can attain better HER activity relative to the more abundant hexagonal counterpart [35].

Vanadium compounds are promising candidates for HER and other electrochemical applications owing to their stable and various oxidation states (V^{2+} to V^{5+}) and high corrosion resistance [29, 36, 37]. Bulk charge transport herein occurs through electron jumps from V^{4+} to O to V^{5+}, and the introduction of V^{4+} within the lattice results in V^{5+} and V^{4+} mixed valance states that boost its intrinsic electrical conductivity [33]. Typically, however, pristine V_2O_5 (pV_2O_5) is not suitable for many electrochemical applications due to its poor stability, low electrical conductivity, and slow electrochemical kinetics [38]. The majority of relevant literature clearly demonstrate that V_2O_5 has been thoroughly examined in comparison to its oxygen deficient counterparts, including V_2O_3 and V_3O_7 [17, 30, 39]. Several types of vanadium-based materials have been investigated as electrocatalysts for acidic HER [40–43], including VO_2 nanorods [44], vanadium oxides with intermediate stoichiometry ($V_{10}O_{24}.nH_2O$) nanofibers [33], and oxygen-deficient V_2O_3 nanoparticles [45]. However, to the best of our knowledge, there are not many reports that have used V_2O_5 electrocatalyst for HER in an alkaline medium.

Herein, we systematically investigate the dual synergism between TM-based doping and oxygen vacancies on V_2O_5-based electrocatalysts in alkaline media towards HER. Unlike in conventional acidic HER, herein, it was found that oxygen deficiencies atop V_2O_5 or Zn-doped V_2O_5 result in a lowering of the electroactivity. Compared to pV_2O_5, $Zn_{0.4}V_{1.6}O_5$ attained 32% lower energy requirement due to an overpotential of -194 mV at -10 mA/cm^2 of current density. Material and electrochemical characterization demonstrated enhanced ECSA, conductivity, kinetics, and hydrophilicity on the optimized catalyst. Moreover, DFT calculations revealed the creation of new electronic states near the Fermi level, lowered bandgaps (i.e., more facile electronic mobility), and more thermodynamically favorable affinity towards HER upon doping and/or anionic deficiencies. The non-polar (110) facets of V_2O_5 were found to be energetically favorable towards HER, which was experimentally confirmed.

2 Experimental

2.1 Materials

Ammonium metavanadate (NH_4VO_3), hydrochloric acid (HCl), oxalic acid ($C_2H_2O_4$), potassium hydroxide (KOH), sodium borohydride ($NaBH_4$), urea ($CO(NH_2)_2$), and zinc

Scheme 1 Synthesis route of V_2O_5@NF or $TM_xV_{2-x}O_5$@NF
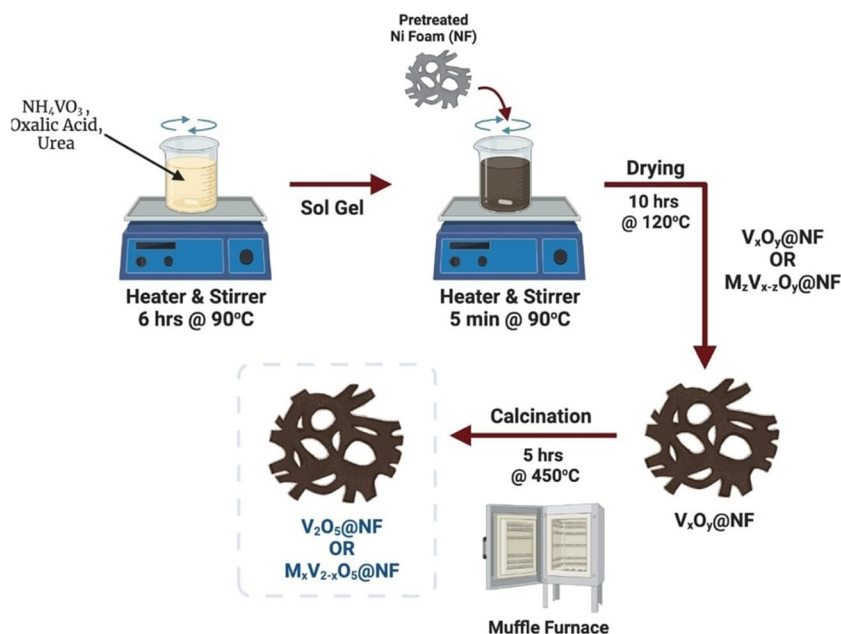
acetate dihydrate ($Zn(CH_3COO)_2 \cdot 2H_2O$) were all purchased from Sigma-Aldrich. KOH was dissolved in deionized water (DIW) to acquire the desired molar concentration of alkaline electrolyte. DIW for all experiments was obtained using the Millipore (18.2 MΩcm) purified water system.

2.2 Synthesis of pristine and Zn-doped V_2O_5

Both pV_2O_5 and $Zn_xV_{2-x}O_5$ electrocatalysts were synthesized using an adapted sol–gel method [46]. Based on preliminary screening syntheses and experiments to ascertain ideal dopant levels, $Zn_xV_{2-x}O_5$ was fabricated using a dopant stoichiometry of $x = 0.4$. Using ammonium metavanadate (NH_4VO_3) as the precursor for V_2O_5, 5.8 g of NH_4VO_3 was dissolved in 50 mL of DIW, and the mixture was continuously stirred for 20 min. Added to the initial mixture as a reducing agent and to maintain the pH to approximately 3 were 1.0 M oxalic acid and 2.0 M of urea. The solution was continuously agitated under heating (90 °C) for 6 h, ensuring gelation. The resultant gel was calcined at 450 °C for 5 h, dried overnight at 120 °C in a programable oven, and crushed to powder form. The same procedure was followed for the preparation of $Zn_{0.4}V_{1.6}O_5$ with the addition of the dopant metal salt, namely, $Zn(CH_3COO)_2 \cdot 2H_2O$, in the initial step with NH_4VO_3. This procedure is depicted and summarized in Scheme 1.

To fabricate the working electrodes, a (1×3) cm^2 piece of porous nickel foam (NF) was pretreated through tip sonication for 1 min in 3.0 M HCl and DIW. Once dried, the NF piece was dipped into the quasi-amorphous phase of the sol–gel solution for 5 min and then dried at 120 °C

overnight. The same calcination procedure was then undertaken as noted.

2.3 Synthesis of reduced V_2O_5 and reduced Zn-doped V_2O_5

Reduction of the as-prepared pristine V_2O_5 to oxygen-deficient V_2O_5 (R-V_2O_5) and reduction of the $Zn_{0.4}V_{1.6}O_5$ (R-$Zn_{0.4}V_{1.6}O_5$) was undertaken through the same strategy. Briefly, an optimized 1:1 molar ratio of $NaBH_4$:M_2O_5 (where M corresponds to metals, i.e., V and Zn) was physically mixed in solid-state for homogenous dispersion of $NaBH_4$ within the powdered metal oxide. This was then moved to a programmable tubular reactor at 450 °C for 1 h of reaction time under Argon flow (20 sccm) to induce anionic oxygen vacancies, at a ramp-up rate of 10 °C/min.

2.4 Structural characterization

A variety of characterization techniques were employed to characterize all fabricated samples. The crystallinity of the samples was assessed by employing an X-ray diffractometer (Rigaku Ultima IV Multipurpose X-ray Diffractometer). Cross-beam optics, a fixed monochromator, and a scintillation counter are incorporated with the diffractometer. XRD radiation source was used at 40 kV and 40 mA, the Cu-Ka. There were four slits used: a scattering slit (2/3°), a divergence slit (2/3°), and a receiving slit (0.3 mm). The XRD data are acquired in continuous scan mode with a step width of 0.02° and 0.5°/min scan speed in the 2θ range of 10–80°. The average crystallite size of the samples was approximated using the Scherrer equation [47], and the particle size of

the samples was analyzed using zeta potential/particle sizer NICOMP™ 380 ZLS technology. Using a field emission scanning electron microscope (FESEM; FEI/ThermoScientific ApreoS), images of the surface morphology were captured at a low acceleration voltage, typically 2 kV. Both an ETD and an in-lens immersion detector were incorporated with the FESEM. High-resolution elemental X-ray photoelectron spectra (i.e., vanadium 2p, oxygen 1 s, and zinc 2p) were collected with a pass energy of 20 eV and a step size of 0.1 eV for pristine, TM-doped, and oxygen-deficient V_2O_5-based samples using an AXIS Ultra DLD X-ray photoelectron spectroscopy (XPS). This surface analysis was conducted for both the as-prepared and postmortem HER electrocatalysts to study potential changes in the surface chemistry during electrochemical operation. The operating conditions for the XPS Al mono (Kα) radiation (1486.6 eV) source were 15-kV and 15-mA emission current. Through deconvolution or peak fitting using Origin-Pro of the high-resolution spectra for the elements of interest, surface chemistries of the samples can be ascertained. Solid-state absorption spectra were collected through UV–Vis-NIR diffuse reflectance spectroscopy (DRS) with a PerkinElmer Lambda 950 Spectrophotometer in the range of 300–800 nm. The bandgaps (E_g) of the V_2O_5-based electrocatalysts were then obtained using the Tauc relation noted in Eq. (1) [48, 49].

$$\alpha h\nu = A\left(h\nu - E_g\right)^n \tag{1}$$

where n equals 3/2 for semiconductors with direct forbidden bandgaps, α is the absorption coefficient, A is a constant, h is Planck's constant, and ν is the photon frequency.

2.5 Electrochemical measurements

All electrochemical measurements were carried out using a standard three-electrode system via a Gamry Reference 3000 potentiostat electrochemical workstation (Gamry, PA, USA) at room temperature and 1.0 M KOH aqueous solution. The counter and reference electrodes employed were a graphite rod and Ag/AgCl electrode, respectively. NF substrates with a V_2O_5-based electrocatalyst atop acted as a working electrode. Regardless of the electrolyte, linear sweep voltammetry (LSV) polarization data were captured at a scan rate of 5 mV/s and a step size of 2 mV. The same step size was used to record cyclic voltammetry (CV) polarization data, but a scan rate of 10 mV/s was used. The Nernst equation (Eq. (2)) was used to convert all measured potentials with respect to reversible hydrogen electrode (RHE) as presented. The Tafel equation (Eq. (3)) was used to fit the linear sections of the Tafel plots to obtain Tafel slopes (b).

$$E(RHE) = E(Ag/AgCl) + (0.059 \times pH) + 0.197V \tag{2}$$

$$\eta = b\log(j) + a \tag{3}$$

where η is the overpotential in mV, j is the current density in mA/cm^2, and b is the Tafel slope in mV/dec. Current stabilization was ensured prior to LSV collection by running at least five cycles of CV. Chronoamperometry (CA) stability tests were conducted by fixing the potential at a predetermined value and recording any divergence in the resultant current density with respect to time. Using Nyquist plots from electrochemical impedance spectroscopy (EIS), the uncompensated resistances (R_u) were determined to apply 90% iR corrections to the LSV polarization curves. From fitting the same Nyquist plots, obtained in the frequency range of 1 MHz to 1 Hz, and at an amplitude AC voltage of 10 mV, the determination of the charge transfer resistance (R_{ct}) of each electrocatalyst is obtained. The R_{ct} is a direct indicator of the conductivity of the electrocatalytic working electrode in relation to other working electrodes tested under the same experimental setup. Evaluation of the Faradaic efficiency (FE) was done using the ratio between the theoretical calculated and experimentally measured gas output during CA tests. The latter was attained through in situ measurements of effluent gas concentration using an on-line gas chromatography (GC) setup. Equations (4–7) describe how FE was calculated:

Theoretical H$_2$ evolution:

$$\dot{n}_{H_2} = \frac{I}{zF} \tag{4}$$

where $\dot{n}_{H_2}$ is the molar flow rate of H_2 produced, I denotes the total amount of current in Ampere, z denotes the moles of electron (i.e., 2 for HER), and F is the Faraday constant (96,485.3 s·A/mol).

$$\dot{n}_{Ar} = \frac{\dot{V}P}{RT} \tag{5}$$

where $\dot{n}_{Ar}$ is the molar flow rate of the carrier gas, $\dot{V}$ denotes the volumetric flow rate of the Argon carrier gas in m^3/s, P denotes the pressure of the gas in Pa, R denotes the ideal gas constant (8.314 kg·m^2/gmol·K), and T denotes the temperature in K.

The theoretical gas concentration is then determined as shown in Eq. 6, and the FE is determined using Eq. 7 as shown:

$$C_{gas,theoretical}(\%) = \frac{\dot{n}_{H_2}}{\dot{n}_{Ar} + \dot{n}_{H_2}} \times 100 \tag{6}$$

$$FE(\%) = \frac{C_{gas,measured}}{C_{gas,theoretical}} \times 100 \tag{7}$$

The experimental concentration of H_2 ($C_{gas,measured}$) produced by the working electrode was measured using the on-line GC every hour for the first 4 h and then every 15 min for the last hour of CA stability tests at -0.39 V (vs. RHE) in 1.0 M KOH. ECSA was determined through the double-layer capacitance (C_{DL}) method at a non-ohmic potential range to generate C_{DL} values from the slope of ascending current density versus scan rates from 5 to 160 mV/s.

2.6 Computational methods

Utilizing the Vienna ab initio simulation package (VASP), the Perdew-Burke-Emzerhof (PBE) functional and exchange correlation (XC) function, spin-polarized DFT computations were performed under the generalized gradient approximation (GGA) [50]. The projected augmented wave (PAW) method [51] was used to treat electron–ion interactions. A plane wave basis set was used to expand the Kohn–Sham orbitals, and the kinetic cutoff energy was optimized at 520 eV. Structural convergence conditions were considered when the Hellmann–Feynman forces and energies were smaller than 10^{-6} eV Å^{-1} and 10^{-4} eV per atom, respectively. The convergence of states towards the system-dependent Fermi levels was accelerated using Gaussian smearing with a finite temperature width of 0.1 eV. In order to perform density of states (DOS) calculations on the bulk systems, a $7 \times 7 \times 7$ k-point mesh created by the Monkhorst–Pack (MP) method was used to sample the Brillouin zone (BZ) [51]. The number of slabs in relation to the specific surface energy (eV Å^{-2}) for each facet was plotted to determine the ideal slab size. Consequently, it was determined that the conditions for specific surface energy convergence are met at four layers with a $3 \times 3 \times 3$ supercell for facet dependency and for H* and H_2O* adsorption investigations, where (*) denotes an active site on the catalytic surface. Further, a conventional 16-Å vacuum region has been added to prevent unphysical interactions. The four atomic slab layers, with a total of 160 atoms, were fully relaxed during the construction of all slabs, and surfaces were built using pre-relaxed bulk cells using VESTA software. For H* or H_2O* adsorption calculations, the bottom two slab layers were artificially fixed in place to represent bulk behavior. The hydrogen binding energy (ΔE_{H^*}) obtained at 0 K (Eq. (8)) was obtained, followed by the corresponding Gibbs free energy change ((ΔG_{H^*})).

$$\Delta E_{H^*} = E[(H^*)] - E[*] - 0.5E(H_2) \tag{8}$$

where $E[(H^*)], E[*]$, and $E(H_2)$ denotes the energies of H adsorbed on the catalyst surface, the energy of the catalyst surface, and the energy of diatomic hydrogen in the gas phase, respectively. ΔG_{H^*} is then obtained from ΔE_{H^*} through accounting for vibrational and entropic changes [52] at 298 K, as shown in Eq. (9).

$$\Delta G_{H^*} = \Delta E_{H^*} + \Delta ZPE - T\Delta S = \Delta E_{H^*} + 0.29eV \tag{9}$$

where ΔZPE is the zero-point energy difference of the species in adsorbed and gas phase. The third term ($T\Delta S$) represents the contribution of the adsorbed intermediate to entropy under experimental conditions [52]. Equation (10) was used to compute the adsorption energy that accompanies the stabilization of H_2O in molecular form. $E_{tot}(V_xO_yH_2O)$ denotes the total energy of the slab that has an adsorbed H_2O molecule, whereas $E_{tot}(V_xO_y)$ denotes the total energy of the pristine slab, and $E_{tot}(H_2O)$ denotes the total energy of the ground state of H_2O [53].

$$E^{ads}(H_2O) = E_{tot}(V_xO_yH_2O) - [E_{tot}(V_xO_y) + E_{tot}(H_2O)] \tag{10}$$

Equations (11–12) were used to calculate the energy and free energy associated with water dissociation. $E_{tot}(V_2O_5OHOH)$ stands for the total energy of the cluster with two OH groups, one of which will be formed by hydrogen stabilization at the surface O and the other by bonding a hydroxyl to the closest vanadium (V) site, both of which are derived from H_2O [53].

$$E_{diss}^{ads}(H_2O) = E_{tot}(V_xO_yOHOH) - [E_{tot}(V_xO_y) + E_{tot}(H_2O)] \tag{11}$$

$$\Delta G_{H_2O^*} = \Delta E_{H_2O^*} + \Delta ZPE - T\Delta S \tag{12}$$

Vacancy (O_v) formation energies for both electrocatalysts were determined through Eq. (13):

$$E_{form} = E_p - E_r + 0.5E_{O_2} \tag{13}$$

where E_{form} denotes the formation energy per oxygen vacancy (O_v) site, E_p denotes the total energy of the pristine system, E_r denotes the total energy of the reduced (oxygen vacant) system, and E_{O_2} is the energy of the diatomic oxygen (O_2) that was obtained from a $10 \times 10 \times 10$ supercell with a $1 \times 1 \times 1$ k-point mesh. Similarly, formation energy associated with TM doping of V_2O_5 was calculated using Eq. (14) to shed light on energetic favorability of Zn doping [54].

$$E_{form,d} = E_{dopedV_2O_5} - E_{pristineV_2O_5} + E_{dopantatom} \tag{14}$$

where $E_{form,d}$ is the energy of formation of doping, $E_{dopedV_2O_5}$ denotes the total energy of the doped system, $E_{pristineV_2O_5}$ denotes the total energy of the pristine system, and $E_{dopantatom}$ is the total energy of the dopant atom.

3 Results and discussion

3.1 Textural and crystallinity characterization

Surface or bulk modulation of transition metal oxides (TMOs), such as pV_2O_5, is known to alter electronic, structural, and surface properties, potentially leading to improved catalytic activity for HER. Specifically, we have previously showcased that electronic conductivity is more favorable when a certain degree of oxygen deficiency (O_v) is established in TMOs [34]. Utilizing XRD, the crystalline structure, purity, and phase composition of the synthesized pristine and reduced electrocatalysts was initially investigated as showcased in the XRD spectra of pV_2O_5, and $Zn_{0.4}V_{1.5}O_5$, and their reduced counterparts, in Fig. 1. The XRD spectra of pV_2O_5 exhibited standard diffraction peaks at 2θ of 15.48°, 20.36°, 21.82°, 26.26°, 31.18°, 32.48°, and 34.40° corresponding to the (200), (001), (101), (110), (301), (011), and (310) facets of standard orthorhombic V_2O_5, respectively, as per JCPDS 41–1426 [55]. Similarly, a control pristine ZnO (pZnO) sample was synthesized through the same sol–gel calcination method, wherein the standard diffraction peaks at 2θ of 31.86°, 34.48°, 36.34°, 47.60°, 56.80°, and 62.94° correspond to the wurtzite ZnO phase [34]. Although the XRD pattern of $Zn_{0.4}V_{1.6}O_5$ demonstrates the maintenance of the predominant V_2O_5 phase, a notable phase distortion is identified, wherein apparent shifts are observed at standard ZnO facet diffraction locations. The resultant induction of lattice distortions, primarily herein in the form of lattice strain, upon Zn-doping results in peak shifts to lower 2θ. Adding to this, the monoclinic phase of $Zn_3(VO_4)_2$ (JCPDS card No: 34–0378) is also apparent at 2θ of 27.38° for both the

pristine and reduced Zn-doped samples, suggesting effective doping [56]. Moreover, it could be seen that upon reducing both V_2O_5 and $Zn_{0.4}V_{1.6}O_5$, the diffraction peak intensities are notably suppressed, suggesting a decrease in crystallinity. This is anticipated because the development of O_v may cause minor configurational alterations to the surface structure [34]. Further, the full-width-half-maximum (FWHM) of the R-V_2O_5 is smaller compared to the pristine counterpart, which translates to having larger crystals, as confirmed from crystallite size determinations in Table 1. As crystallinity structural evidence for both induction of oxygen vacancies in both reduced electrocatalytic cathodes, two apparent new peaks at 2θ of 18.90° and 27.88° are present, corresponding to V_4O_9 and Na-V_2O_5, respectively [57, 58]. The presence of the Na was most likely brought upon during borohydride reduction, and the Na-V_2O_5 phase is thought to be the result of electrostatic interaction between Na^+ and the negatively charged oxygen-deficient surface of V_2O_5 after reduction. Similarly, the lower ratio of oxygen to vanadium in the V_4O_9 phase correlates to the formation of O_v.

Average crystallite size determination from diffraction patterns in Fig. 1 was undertaken using the modified Scherrer method to shed light on the relation between crystallite size, surface propagation of electrons, and how it relates to the electrochemical results obtained [59]. The presented average crystallite size and particle size in Table 1 demonstrate that induction of O_v through physicochemical reduction increases both parameters. Initially, this suggested that reduction would have advantageous electrocatalytic properties due to a large crystallite size typically correlating to unhindered surface propagation of electrons, not necessarily conductivity. This is because surface and bulk conductivities also depend on the intrinsic conductivity of the TMO phase, such as but not limited to its bandgap. Notwithstanding, Zn doping of the pristine V_2O_5 sample resulted in a notable drop from approximately 42.2 to 33.7 nm in the crystallite size, potentially due to the aforementioned lattice distortion effects during Zn doping on the orthorhombic host crystal. Of note, however, the average crystallite size is the largest for the reduced $Zn_{0.4}V_{1.6}O_5$, suggesting a significant phase transformation.
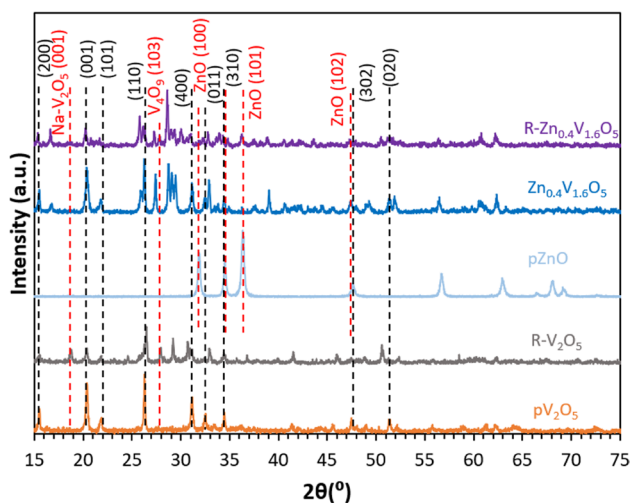
Fig. 1 a X-ray diffraction (XRD) spectra of as-synthesized pV_2O_5, R-V_2O_5, pZnO, $Zn_{0.4}V_{1.5}O_5$, and R-$Zn_{0.4}V_{1.6}O_5$

Table 1 Scherrer approximated average crystallite size and measured particle size of as-prepared TMOs

| Electrocatalysts	Average crystallite size (nm)	Particle size (µm)
V_2O_5	42.2	0.397
R-V_2O_5	43.3	0.506
$Zn_{0.4}V_{1.6}O_5$	33.7	0.288
R-$Zn_{0.4}V_{1.6}O_5$	47.2	0.430

FESEM images were taken at 50,000 × magnification to investigate the resultant morphologies of the as-prepared V_2O_5-based electrocatalysts, as shown in Fig. 2. It can be observed that there is an aggregation of particles with different sizes and irregular morphologies, comprising of rounded corners and sharp edges. A general inference can be made from this observation that the presence of Zn dopants does not alter the resultant morphology, namely, due to the utilized sol–gel calcination procedure dictating the morphology of the predominant V_2O_5 electrocatalyst. Comparing Fig. 2a and 2c for pV_2O_5 and $Zn_{0.4}V_{1.6}O_5$, respectively, it can be seen that lower aggregation and larger dimensionality are present in the Zn-doped counterpart. Further, FESEM images of the reduced electrocatalysts in Fig. 2b and d demonstrate more unidimensional rod-shaped particles of larger surface area and size relative to their pristine counterparts, as confirmed from Table 1. This translates to the reduced samples having, on average, larger crystallite sizes, and their larger crystals translate to larger surface conductivities and lower resistance from crystal domain breaks. Therefore, this initially implied that based on crystallite conductivity effects alone, the HER activity of the reduced electrocatalysts should be greater than their pristine counterparts since HER favors more conductive electrocatalysts. To confirm the homogeneity of the doping procedure and investigate whether typically undesired phase separation phenomena were at play, energy-dispersive X-ray spectrometry (EDS) as an accessory to the FESEM analysis was undertaken. Figures S1-S4 demonstrate that uniform distribution of the V and O, and Zn for the two doped samples, was present.

3.2 Electrochemical performance towards HER in alkaline environments

The alkaline HER performance of the as-prepared electrocatalysts atop NF was investigated in a standard three-electrode cell under 1.0 M KOH electrolyte. Polarization curves in Fig. 3a showcases overpotential requirements for pV_2O_5@NF, R-V_2O_5@NF, $Zn_{0.4}V_{1.6}O_5$@NF, and R-$Zn_{0.4}V_{1.6}O_5$@NF at − 256, − 312, − 194, and − 258 mV, respectively, at 10 mA/cm^2 of current density. It can clearly be noted that modulation of pV_2O_5@NF or $Zn_{0.4}V_{1.6}O_5$@NF through introduction of anionic deficiencies is found to be disadvantageous to the alkaline HER activity. Contrarily, a 32% enhancement in electroactivity is observed for the $Zn_{0.4}V_{1.6}O_5$@NF relative to its undoped pV_2O_5@NF counterpart. To investigate this, electrocatalytic conductivity is first compared from charge transfer resistance (R_{ct}) measurements obtained from EIS Nyquist plots, performed at an applied potential corresponding to − 10 mA/cm^2 of current density, as shown in Fig. 3b. It is observed that in fact $Zn_{0.4}V_{1.6}O_5$@NF with the highest electroactivity demonstrates the lowest R_{ct} value of 2.54Ω, suggesting highest bulk conductivity of the investigated samples. Further, the results suggest that although reduction results in an increase in crystallite size, the resultant changes to bulk electronics are more detrimental towards the conductivity of the material. It is worth noting that under alkaline conditions, the feed reactants for HER are in fact water molecules that first need to be dissociated onto the surface of the cathode prior to Tafel recombination or Heyrovsky reduction. Moreover, as shown from XRD results, upon doping pV_2O_5 with cationic $Zn^{\delta+}$, lattice distortions may result in subtle rearrangement to the

Fig. 2 FESEM images for prepared vanadium pentoxide powders: **a** pV_2O_5, **b** R-V_2O_5, **c** $Zn_{0.4}V_{1.6}O_5$, and **d** R-$Zn_{0.4}V_{1.6}O_5$
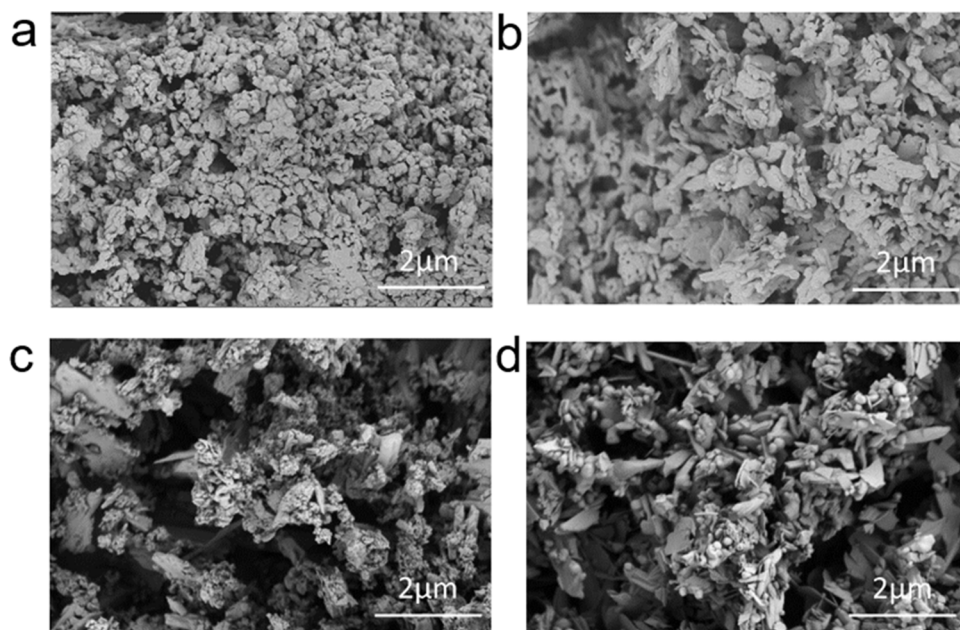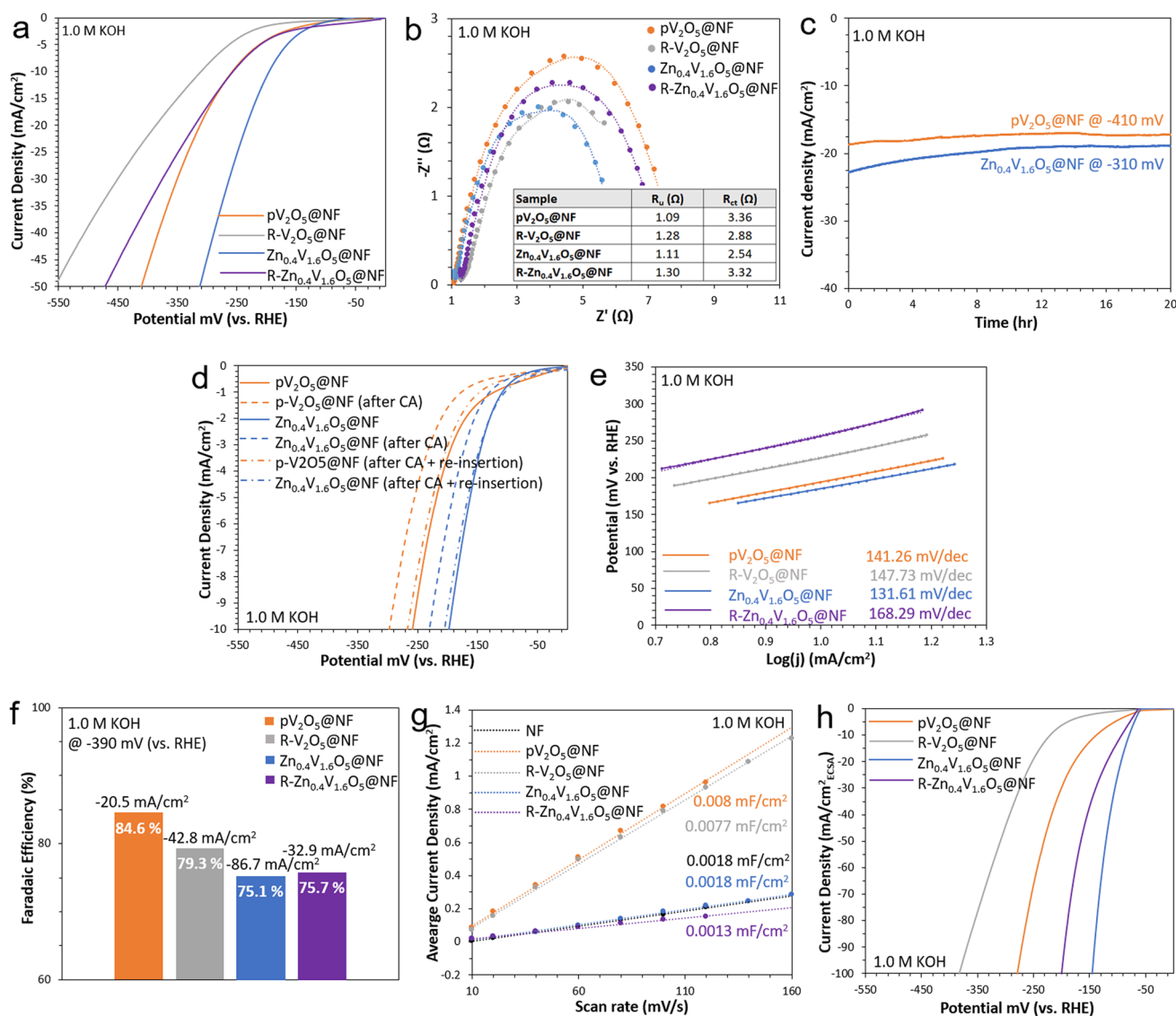
Fig. 3 a LSV polarization curves and **b** EIS Nyquist plots for $pV_2O_5@NF$, R-$V_2O_5@NF$, $Zn_{0.4}V_{1.6}O_5@NF$, and R-$Zn_{0.4}V_{1.6}O_5@NF$ in alkaline electrolyte. **c** Chronoamperometry (CA) stability plots and **d** LSV polarization curves for $pV_2O_5@NF$ and $Zn_{0.4}V_{1.6}O_5@NF$ before-after CA and after re-insertion into electrolyte. **e** Tafel slopes, **f** Faradaic efficiencies at -390 mV, **g** double-layer capacitance (C_{DL}) measurements, and **h** ECSA-normalized LSV polarization curves for $pV_2O_5@NF$, R-$V_2O_5@NF$, $Zn_{0.4}V_{1.6}O_5@NF$, and R-$Zn_{0.4}V_{1.6}O_5@NF$ in alkaline electrolyte

crystal structure. This causes the size and shape of the unit polyhedral to alter, effectively leading to deformation of the unit pyramidal chains. The cathodic surface becomes more porous with denser grain boundaries as the $Zn^{\delta+}$ dopant in V_2O_5 increases, as shown by a decrease in average crystallite size from pV_2O_5 (42.2 nm) to $Zn_{0.4}V_{1.6}O_5$ (33.7 nm) making it easier for dissociated protons to react in the latter. From a mechanistic view, one possible explanation for the suppressed electroactivity upon the introduction of O_v can be envisaged from the partially positive charge of the O_v site which under alkaline conditions is stabilized by electrostatically attracting anionic hydroxides from solution.

The resultant highly anionic surface of the reduced samples may disadvantageously bind too strongly with $H^{\delta+}$ of water molecules ($H^{\delta+}$–$OH^{\delta-}$), without abundance of cationic sites on the surface to bind with $OH^{\delta-}$ from water, since they are kinetically more likely to bind with electrolytic hydroxide. Importantly, we believe the increased difference in electronegativity between cationic $[ZnV]^{\delta+}$ and anionic $[O_y]^{\delta-}$ for the $Zn_{0.4}V_{1.6}O_5$ surface, as opposed to the pV_2O_5 surface, enhances the dissociation kinetics of water. We have recently demonstrated this through a surface-heterointerfaced electron-localized NiV and Co-(NiFe) oxynitride cathodic and anodic surfaces, respectively, under neutral pH electrolysis

wherein water dissociation is also typically rate-determining [60, 61].

Furthermore, to test the electrochemical stability of the as-prepared cathodes, CA analyses were conducted over 24 h at an initial current density of -50 mA/cm^2. As shown in Fig. 3c, only 20-h stability plots are presented due to the rapid decrease in current density in the first 4 h as a result of an experimental artifact from micro- and nano-bubble buildup on the rough catalytic surface which create high interfacial resistances [62]. To demonstrate this point, we generated the polarization curves shown in Fig. 3d before and after CA, which showcase the electroactivity decay. However, in the same Fig. 3d, momentarily taking the electrodes out of the electrolyte to detach micro-bubbles near active sites and re-inserting them back in the initial electroactivity is largely restored. To look into the kinetics at play, Tafel slopes (Fig. 3e) were generated from the respective polarization curves. However, the attained Tafel slopes are quite large corresponding to Volmer-limited kinetics, which could potentially be due to a poor heterojunction between the V$_2$O$_5$-based catalysts and the underlying NF. This would in turn result in undesired resistance between the active catalytic surface and the porous conductive NF substrate, which can be related to the Rct values obtained from the Nyquist plots in Fig. 3b.

To investigate the Faradaic efficiency (FE) of the developed cathodes, on-line GC measurements at pre-specified time intervals were undertaken during 5-h CA tests at the same applied potential of -390 mV (vs. RHE) for all catalysts. The summarized average FE results in Fig. 3f suggest at first glance that the highest efficiency corresponds to the undoped pV$_2$O$_5$@NF, wherein 84.6% FE for HER was recorded. However, it is important to correspond the measured FE with the resultant current density under operation for each respective catalyst since it is well known that FE tends to decrease with respect to an increasing current density. To that end, when reporting the 75.1% measured FE for Zn$_{0.4}$V$_{1.6}$O$_5$@NF, it is important to note that this is at -86.7 mA/cm^2 of current density, compared to 84.6% FE for pV$_2$O$_5$@NF but at a quarter of the aforementioned current density. Moreover, to determine the intrinsic electroactivity of the developed electrocatalysts, the ECSA-normalized polarization curves are investigated. First, electrocatalyst-dependent ECSAs were calculated using the relationship between the double-layer capacitance (C$_{DL}$) and the specific solution capacitance of alkaline electrolyte (C$_S$ = 0.04 mF/cm^2). CV measurements at different scan rates from 5 to 160 mV/s were conducted in non-Faradaic potential region, as shown for all prepared electrocatalysts presented in Figure S5. The average current densities at the potential-midpoint were then plotted with respect to scan rate in Fig. 3g, whereby the slopes correspond to the catalyst-specific C$_{DL}$, shown in Fig. 3g. To that end, LSV

polarization data from Fig. 3a was normalized with respect to ECSA in Fig. 3h. It can be observed that although the Zn$_{0.4}$V$_{1.6}$O$_5$@NF electroactivity is still the highest, confirming it to be the most electroactive intrinsic surface investigated, R-Zn$_{0.4}$V$_{1.6}$O$_5$@NF is now the second highest in terms of intrinsic activity. The attained comparison suggests that although pV$_2$O$_5$@NF has the highest ECSA, the modulated surfaces of both Zn$_{0.4}$V$_{1.6}$O$_5$@NF and its reduced counterpart are more intrinsically favorable towards alkaline HER.

3.3 Surface chemical characterization

To probe the changes in the surface chemical states, high-resolution XPS spectral measurements on the two pristine oxides, namely, pV$_2$O$_5$@NF and Zn$_{0.4}$V$_{1.6}$O$_5$@NF, were undertaken both for the as-prepared materials and after the cathodic chronoamperometric HER of Fig. 3c. Using the Shirley background subtraction method and Gaussian fitting, deconvolution of the O 1 s spectra are showcased in Fig. 4a. As can be seen, pV$_2$O$_5$@NF and Zn$_{0.4}$V$_{1.6}$O$_5$@NF have an initial notable peak at 529.2 and 529.1 eV, respectively, corresponding to lattice oxygen sites, and subtle shoulder peaks for both samples at binding energies of approximately 530.5 and 531 eV corresponding to defective and low coordination oxygen (M-OH, wherein M represents both V and Zn sites) on the surface, respectively [63, 64]. As eluded to earlier, atomic-thin semiconducting hydroxide surface may enhance the water dissociation kinetics during alkaline HER [65]. It is important to recall that XPS scans the top 5–10 nm of the surface, and therefore, the apparent higher ratio of surface-bound hydroxide to lattice oxygen in post-HER O 1 s spectra of pV$_2$O$_5$@NF suggests that low conductivity is expected, compared to the post-HER O 1 s spectra of Zn$_{0.4}$V$_{1.6}$O$_5$@NF which shows the opposite ratio. This is corroborated from the R$_{ct}$ values showcased in Fig. 3b during EIS analysis. The V 2p spectral analysis in Fig. 4b reveals a clear distinction among the as prepared and post-HER samples. Firstly, the V 2p spectra for the pV$_2$O$_5$@NF matches exceptionally well with the standard binding energy positions for the ground state V$^{5+}_{3/2}$ and V$^{5+}_{1/2}$ corresponding to 517.1 and 524.5 eV, respectively [66]. In agreement with the XRD analysis, an approximate 0.3 eV shift towards higher binding energy is noted for the same peaks in the as-prepared Zn$_{0.4}$V$_{1.6}$O$_5$@NF, suggesting lattice strain as a result of the dopant Zn species. Further, post-HER analysis in both catalysts showcases peaks corresponding to the V$^{3+}_{3/2}$ and V$^{3+}_{1/2}$ states as a result of the reducing environment on the cathode surface and suggestive that the active sites herein are vanadium atoms. Notwithstanding, it can be observed that smaller degree of the V^{3+} is noted for the post-HER Zn-doped sample. This is expected to be a result of the Zn doping wherein the more electronegative Zn is postulated to synergistically withdraw electrons from neighboring V sites,
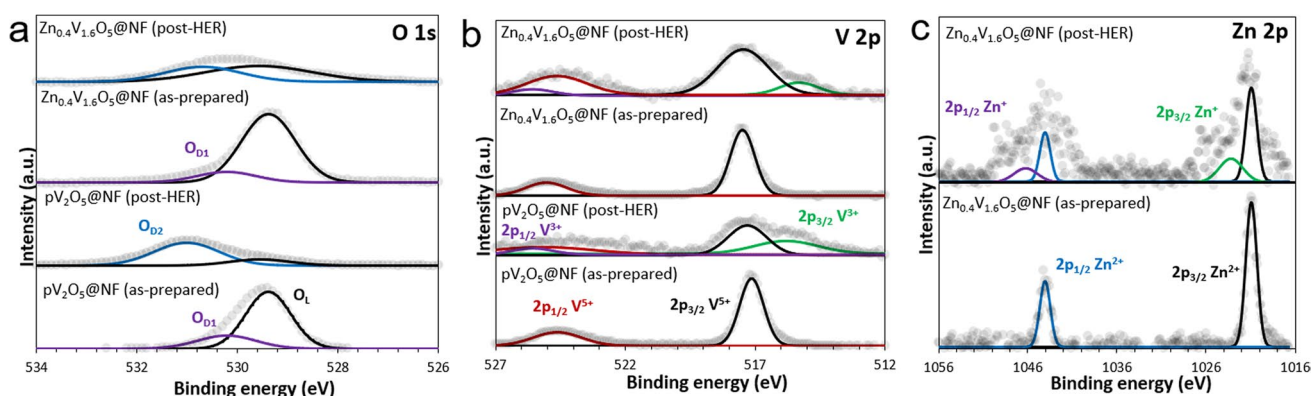
Fig. 4 **a** High-resolution XPS spectra for O 1 s, **b** V 2p, and **c** Zn 2p for the pristine as-prepared pV$_2$O$_5$@NF and Zn$_{0.4}$V$_{1.6}$O$_5$@NF and after 24-h chronoamperometric HER (post-HER)

thereby maintaining a higher oxidation state for vanadium. This is corroborated from the as-prepared and post-HER Zn 2p spectra in Fig. 3c, whereby a notable degree of the initial Zn^{2+} is reduced to Zn$^+$.

Since water molecules are the initial feed or reactant during alkaline HER, it was important to measure the hydrophilicity associated with the different cathodic electrocatalysts. The contact angles were measured five times at different positions on a glass slide containing drop-casted inks of the electrocatalysts and the average contact angles are shown in TableS1. It can be deduced that upon reduction, the contact angle decreases for both R-V$_2$O$_5$ and R-Zn$_{0.4}$V$_{1.6}$O$_5$ compared to V$_2$O$_5$ and Zn$_{0.4}$V$_{1.6}$O$_5$, meaning that the reduced samples are favorably more hydrophilic. Anomalously, the best-performing alkaline HER sample, namely, Zn$_{0.4}$V$_{1.6}$O$_5$, attained the larger contact angle at 91.66°, relative to R-V$_2$O$_5$ which exhibited the highest hydrophilicity at an angle of 78.10°. Nonetheless, the relatively small variance of ~ 14° between the most and least electroactive cathode suggests that this metric of hydrophilicity is perhaps not as crucial to this catalytic system compared to other metrics such as conductivity and intrinsic site activity.

3.4 DFT calculations

It is of paramount importance to first determine which facets are more energetically favorable towards doping and induction of defects since the governing thermodynamic selectivity will determine where the doping will realistically take place. The bulk structure used to create the five-faceted V$_2$O$_5$ slabs on VESTA is shown in Figure S6 and later used to model the five predominant facets of V$_2$O$_5$, namely, the (001), (002), (101), (011), and (110), in agreement with the attained XRD patterns, as shown in Figure S7. The relaxed slabs were then used for the H* adsorption calculation, whereby a H atom was standardly placed above a lattice V atom at an initial distance of ~ 1.5Å (Figure S8)

more than the distance of a V–O bond length, whereby the V top-site is assumed to be the active site during HER. The Gibbs free energy of hydrogen (ΔG_{H*}) was calculated after slab relaxation and subsequent H* adsorption determination. Thermodynamic reaction coordinate profiles based on ΔG_{H*} calculations on the five faceted V$_2$O$_5$ surfaces was generated as shown in Fig. 5a. Based on the results obtained in Fig. 5a, it can be seen that the two most thermodynamically favorable facets of V$_2$O$_5$ are the nonpolar (002) and (110) facets, yielding ΔG_{H*} values of − 0.55 and − 0.68 eV, respectively. The obtained results and facet-dependent trends with respect to ΔG_{H*} herein are consistent with the reported values in the literature for similar facets [67, 68]. Both the (110) and (002) facets are considered more favorable due to having more surface O group locations in relation to the V top site, which can interact more strongly with the H molecules and stabilize them on the surface. Additionally, the (002) and (110) facets have a more open-top structure, which can also facilitate proton adsorption and desorption. Although diffraction patterns from XRD showcased presence of both (002) and (110) facets, the corresponding FESEM images did not indicate dominant one-dimensional morphologies, which would be expected if the nonpolar (002) was predominant.

Additionally, and of interest to the experimental oxygen-deficient samples, the specific formation energies for a vacancy on each accessible O-type were computed in our previous work on V$_2$O$_5$ because of the high surface density of available oxygen sites in pV$_2$O$_5$—namely, 1-, 2-, and 3-coordinated O types [55]. It was determined that the (110) and (001) facets of the 2- and 1-coordinated oxygens are the most thermodynamically favorable, with formation energies of 0.70 and 0.74 eV per vacancy, respectively. Notwithstanding, and since this work focuses on alkaline HER, H$_2$O adsorption/dissociation calculations were conducted on the (110) and (001) facets to determine which facet is more thermodynamically favorable towards the dissociation of the reactant. From the summarized results in Fig. 5b, it
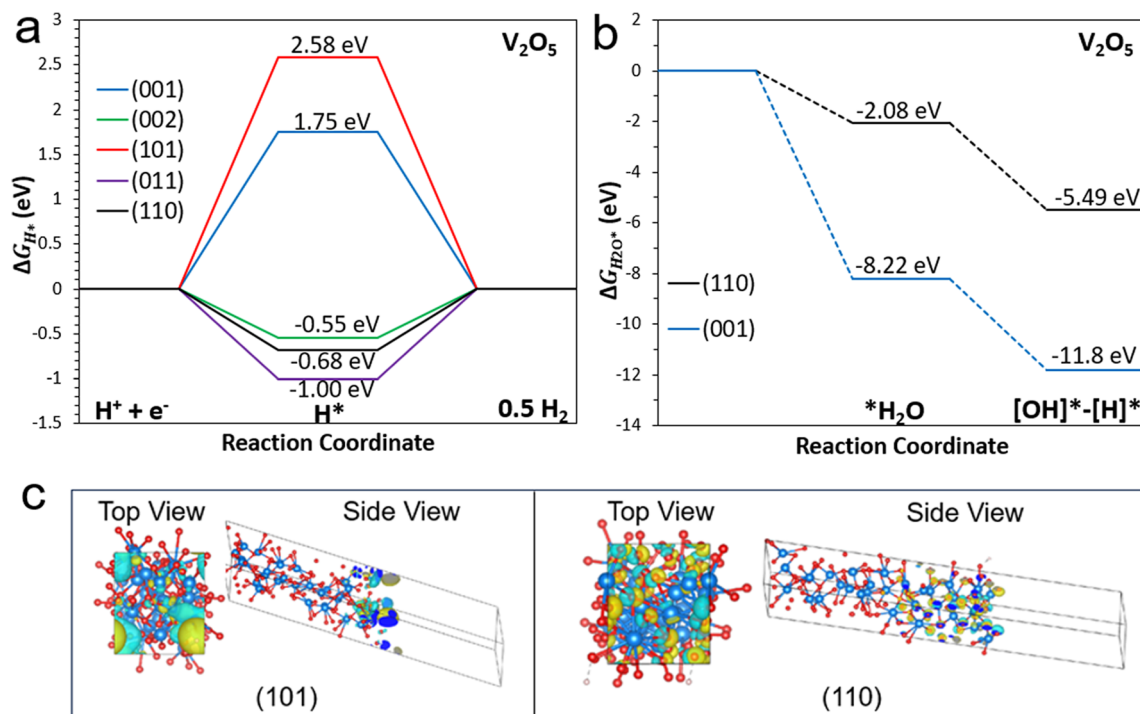
Fig. 5 **a** Gibbs free energy diagrams of hydrogen adsorption and **b** water adsorption/dissociation on select V_2O_5 facets. **c** Charge density difference plots for the (101) and (110) faceted V_2O_5 slabs. Charge accumulation is depicted by the yellow area, and the charge depletion is shown by the cyan area in (**c**)

was determined that for the typically water dissociation rate determining step (RDS), less energy was needed to adsorb H_2O onto the surface of the (110) facet. Therefore, since both (002) and (110) facets have similar formation energies towards anionic deficiencies in their lattice, coupled with (110) being the predominant facet based on XRD and SEM analysis, and more importantly being more energetically favorable towards H_2O dissociation, we opted to model the remaining systems based on the nonpolar (110) facet.

Charge density difference (CDD) plots were generated and investigated to examine the charge redistribution effects from adsorbed H* on the local charge density at the interfacial surface. Figure 5c demonstrates the CDD plots for the least (101) and most (110) energetically favorable facets of V_2O_5 that are being investigated based on the ΔG_{H*}. CDD only typically occurs in the first top two layers of the slab, and the bulk layers have little to no contribution. Around the initial cationic proton approaching the surface, facets with negative adsorptive binding energies expectedly exhibited charge accumulation phenomena. The CDD plots for the remaining faceted slabs are shown in Figure S8. Hydrogen adsorption calculations on the doped and reduced V_2O_5 slabs were done is the same aforementioned manner, where the H atom was placed on the V atom circled green in Figure S9. The energy of formation of the dopant was calculated to determine how likely the doping can occur, and it

was determined that the formation energies of Zn doping was -9.04 eV. The orange circles in Figure S9b(iii) represents the vacant oxygen site, and the exact position was chosen because it was determined that it is much more favorable for anionic vacancies to form on the top surface rather than the second layer for this facet, based on our previous work [55].

The ΔG_{H*} thermodynamic profiles of the four examined slabs are shown in Fig. 6a, and it can be seen that anomalously the R-V_2O_5 slab has the closest binding energy to thermoneutrality counter to the experimental polarization data. On the same seemingly anomalous trends, both pV_2O_5 and $Zn_{0.4}V_{1.6}O_5$ have the most unfavorable ΔG_{H*} results, yet experimentally attain the highest activities. To that end, it is again important to realize that the experimental analysis was conducted in alkaline electrolyte wherein the typically limiting molecular water binding and subsequent dissociation (Fig. 6b) are typically more rate-limiting compared to proton reduction (Fig. 6a). In corroboration with experimental findings, Fig. 6b therefore demonstrates that the water dissociation energetics are more thermodynamically favorable on the pV_2O_5 and $Zn_{0.4}V_{1.6}O_5$. This highly suggests that in fact water dissociation is largely limiting in alkaline conditions as shown previously. In fact, the best experimental activity for $Zn_{0.4}V_{1.6}O_5$ matches the same sample attaining the highest thermodynamic favorability towards water
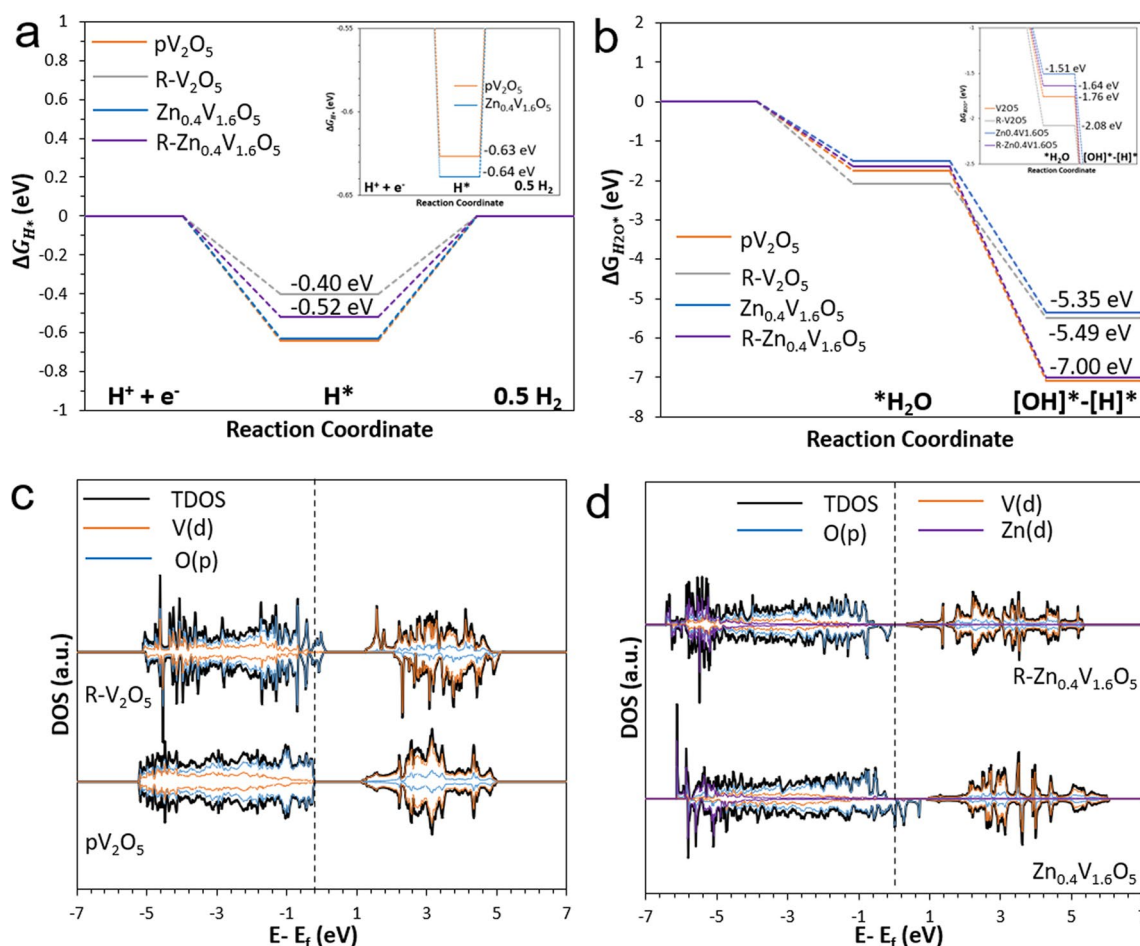
Fig. 6 **a** Gibbs free energy diagrams of hydrogen adsorption, **b** water adsorption/dissociation, and **c** T/PDOS of pV_2O_5, $R-V_2O_5$, $Zn_{0.4}V_{1.6}O_5$ and $R-Zn_{0.4}V_{1.6}O_5$ surfaces

dissociation. Moreover, to investigate why $R-V_2O_5$ gave a near-thermoneutral theoretical binding energy but had poor alkaline experimental HER performance, O_v formation energies (Table S2) were calculated. It can be clearly seen that the formation energy of the anionic vacancy on pV_2O_5 is energetically favorable with a formation energy of approximately -5.3 eV, contrary to that for $Zn_{0.4}V_{1.6}O_5$ being ~ 13.7 eV. Since experimentally both samples underwent the same physicochemical reduction procedure, providing the same energy during the process, the case can be made that the degree of reduction in both samples is different. That is to say that it is more likely to create more vacancies, both favorable surface vacancies and undesired bulk vacancies which may cause structural distortions, in the pV_2O_5 upon reduction to $R-V_2O_5$ which can potentially make the resultant reduced sample unstable and far from the modelled $R-V_2O_5$ system. Bulk O_v not only affects conductivity of the electrocatalyst but may lower stability under harsh electrochemical testing conditions. Large amounts of O_v on the surface promote reaction intermediate adsorption,

whereas excessive O_v in the bulk are undesirable because they disrupt the interaction between cations with different valence states and the uniform movement of electrons [69].

The electron band structure analysis conducted on investigated systems, both pristine and reduced, establishes the presence of an intrinsic indirect bandgap in pV_2O_5. Calculations of total and projected density of state (T/PDOS) were performed using a refined mesh, shown in Fig. 6c and d. The difference between the valence band maximum (VBM) and conduction band minimum (CBM), namely, the bandgap, are found to be in good agreement with the experimentally attained bandgaps from diffuse reflectance spectroscopy (DRS) Tauc plots in Figure S10, particularly for pV_2O_5. The hybridization observed between the 2p and 3d orbitals of oxygen and vanadium, respectively, in the VB region underscores the clear covalent character inherent in lattice V−O bonds. Within pV_2O_5, the VBM predominantly originates from the O p states, with the contribution of the V d states becoming more prominent as we move away from the Fermi level. Creation of new electronic states near the Fermi

level are clearly note upon reduction from pV_2O_5 to R-V_2O_5, which are typically advantageous towards hydrogen binding energies—as was noted for R-V_2O_5 in Fig. 6a. The same trend is also observed for the Zn-doped system and upon its reduction, with a clear decrease in bandgaps (Table 2), indicative of higher conductivity which was also confirmed experimentally from R_{ct} determination of EIS Nyquist plots in Fig. 3b [70]. Further, for $Zn_{0.4}V_{1.5}O_5$ and R-$Zn_{0.4}V_{1.5}O_5$, the O-p and Zn-d states are primarily responsible for the VBM, while the V-d mainly contributes more for the CBM. Presence of defect states from dopants or elemental deficiencies in the bandgap can create additional electronic states that can either facilitate or impede electron transfer depending on their energy level and their interaction with the VBM and CBM. Additionally, the electronic states of the conduction band can be filled with a lot of electrons owing to O_v, which can cause the electron states near the Fermi level to shift to higher energies and enhance the activity as more electrons or holes are available for reduction or oxidation closer to the Fermi level. This is seen when V_2O_5 is reduced and its bandgap gets narrowed from 1.33 eV to 1.13 eV, which is a 15% reduction in DOS bandgap. Similarly, for $Zn_{0.4}V_{1.5}O_5$, the DOS attained bandgap decreased from 1.16 eV to 0.92 eV upon reduction. However, due to the intrinsic inaccuracy of the PBE functional in calculating the bandgap of metal oxides, it is not a reliable method to compare its results to experimental values, albeit the trend should be quite similar. Compared to the bandgap obtained from the T/PDOS, the same trend is observed for experimental bandgap measurements calculated from DRS Tauc plot (Figure S10) where the bandgap also narrows when pV_2O_5 gets doped with Zn and once it gets reduced (Table 2).

The CDD was investigated to examine the charge redistribution upon doping or reduction of thepV_2O_5-based electrocatalysts, shown in Figure S11. Again, CDD typically occurs in the first top two layers of the slab, and the bulk layers have little to no contribution. The electrocatalysts with negative binding energies show charge accumulation phenomena in CDD around the initially cationic proton approaching the surface. Ideal charge coordination between the inbound charge of hydrogen and the nearby V atoms results from this charge-depleted local zone acting as a stabilization center. It

can be observed that there is a surface rearrangement caused by the introduction of an O_v to pV_2O_5 and that the oxygen-deficient region shows that the nearby atoms have more charge accumulation. This redistribution facilitates the H adsorption and promotes the HER activity, which was seen from the low ΔG_{H^*} value of R-V_2O_5 in Fig. 6a. In addition, the presence of dopants does results in a noticeable surface rearrangement, albeit charge redistribution is more evident in the reduced electrocatalyst structures. For $Zn_{0.4}V_{1.5}O_5$, there is an observable charge accumulation on the Zn dopant atom and hydrogen atom. This suggests that the charge transfer occurs from the O to the H. Therefore, it can be inferred that the addition of a Zn dopant atom or the removal of an oxygen atom results in clear charge redistribution in the structure of the electrocatalyst which when coupled with binding energy results from Figs. 6a and 6b suggests a clear effect on H* and/or water dissociation. Figure S11 illustrates that the presence of O_v may improve the delocalization of the electrons, resulting in more effective sites for H adsorption. These findings demonstrate that O_v in electrocatalysts might enhance the surface adsorption properties and give additional active sites, allowing them better activity towards HER.

4 Conclusion

We investigated V_2O_5-based electrocatalysts both Zn-doped and reduced samples with oxygen-deficient lattices through a modified sol–gel method coupled with physicochemical reduction towards alkaline HER. Unconventional V_2O_5 was chosen due to its earth abundance, non-toxicity, and relative cost-effectiveness to the conventional Pt-based cathodic benchmark. The intrinsically poor electroactivity of V_2O_5 was an opportunity to systematically investigate the aforementioned effects of dopants and oxygen vacancies. $Zn_{0.4}V_{1.6}O_5$ achieved the lowest overpotential of 194 mV and 310 mV to reach current densities of -10 mA/cm^2 and -50 mA/cm^2, respectively, in 1.0 M KOH. The coupling of DFT and material characterization techniques allowed for the rational deduction of activity trends in the alkaline electrolyte used herein. Online GC measurements were employed towards Faradaic efficiency determination during chronoamperometric stability tests. All in all, conductivity, lattice stability, hydrophilicity, surface energetics towards hydrogen binding, and the typically rate-limiting water dissociation step, coupled with electronic states near the Fermi level, resulted in $Zn_{0.4}V_{1.6}O_5$ attaining the highest performance and a 32% improvement in alkaline HER electroactivity relative to the initial pristine V_2O_5. Observations from theoretical and material-based analyses were synergistically coupled with ECSA-normalized current densities which also showcased that $Zn_{0.4}V_{1.6}O_5$ had the highest intrinsic activity.

Table 2 Experimental and theoretical bandgap of V_2O_5, R-V_2O_5, $Zn_{0.4}V_{1.5}O_5$, and R-$Zn_{0.4}V_{1.6}O_5$

Electrocatalysts	GGA-PBE bandgap (eV)	Experimental bandgap (eV)
V_2O_5	1.33	2.15
R-V_2O_5	1.13	1.45
$Zn_{0.4}V_{1.6}O_5$	1.16	2.24
R-$Zn_{0.4}V_{1.6}O_5$	0.92	1.85

Declarations

References

1. S. Chu, A. Majumdar, Opportunities and challenges for a sustainable energy future. Nature **488**(7411), 294–303 (2012). https://doi.org/10.1038/nature11475

2. B.D. Solomon, K. Krishna, The coming sustainable energy transition: history, strategies, and outlook. Energy Policy **39**(11), 7422–7431 (2011). https://doi.org/10.1016/j.enpol.2011.09.009

3. K.H. Solangi, M.R. Islam, R. Saidur, N.A. Rahim, H. Fayaz, A review on global solar energy policy. Renew. Sustain. Energy Rev. **15**(4), 2149–2163 (2011). https://doi.org/10.1016/j.rser.2011.01.007

4. N.L. Panwar, S.C. Kaushik, S. Kothari, Role of renewable energy sources in environmental protection: a review. Renew. Sustain. Energy Rev. **15**(3), 1513–1524 (2011). https://doi.org/10.1016/j.rser.2010.11.037

5. N.S. Lewis, Toward cost-effective solar energy use. Science **315**(5813), 798–801 (2007). https://www.science.org/doi/10.1126/science.1137014

6. Z. Yang, J. Zhang, M.C. Kintner-Meyer, X. Lu, D. Choi, J.P. Lemmon et al., Electrochemical energy storage for green grid. Chem. Rev. **111**(5), 3577–3613 (2011). https://doi.org/10.1021/cr100290v

7. K.L. Lim, H. Kazemian, Z. Yaakob, W.R.W. Daud, Solid-state materials and methods for hydrogen storage: a critical review. Chem. Eng. Technol. **33**(2), 213–226 (2010). https://doi.org/10.1002/ceat.200900376

8. N.S. Lewis, D.G. Nocera, Powering the planet: chemical challenges in solar energy utilization. PNAS **103**(43), 15729–35 (2006). https://doi.org/10.1073/pnas.0603395103

9. J. Tian, Q. Liu, A.M. Asiri, X. Sun, Self-supported nanoporous cobalt phosphide nanowire arrays: an efficient 3D hydrogen-evolving cathode over the wide range of pH 0–14. J. Am. Chem. Soc. **136**(21), 7587–7590 (2014). https://doi.org/10.1021/ja503372r

10. J.A. Turner, Sustainable hydrogen production. Science **305**(5686), 972–974 (2004). https://doi.org/10.1126/science.1103197

11. G.W. Crabtree, M.S. Dresselhaus, M.V. Buchanan, The hydrogen economy. Phys. Today **57**(12), 39–44 (2004). https://doi.org/10.1063/1.1878333

12. Z. Ge, B. Fu, J. Zhao, X. Li, B. Ma, Y. Chen, A review of the electrocatalysts on hydrogen evolution reaction with an emphasis on Fe, Co and Ni-based phosphides. J. Mater. Sci. **55**(29), 14081–14104 (2020). https://doi.org/10.1007/s10853-020-05010-w

13. A. Eftekhari, Electrocatalysts for hydrogen evolution reaction. Int. J. Hydrogen Energy **42**(16), 11053–11077 (2017). https://doi.org/10.1016/j.ijhydene.2017.02.125

14. K.M. Naik, S. Sampath, Cubic Mo6S8-efficient electrocatalyst towards hydrogen evolution over wide pH range. Electrochim. Acta **252**, 408–415 (2017). https://doi.org/10.1016/j.electacta.2017.09.015

15. J.R. McKone, S.C. Marinescu, B.S. Brunschwig, J.R. Winkler, H.B. Gray, Earth-abundant hydrogen evolution electrocatalysts. Chem. Sci. **5**(3), 865–878 (2014). https://doi.org/10.1039/c3sc51711j

16. R.A. Mir, O.P. Pandey, Influence of graphitic/amorphous coated carbon on HER activity of low temperature synthesized β-Mo2C@C nanocomposites. Chem. Eng. J. **348**, 1037–1048 (2018). https://doi.org/10.1016/j.cej.2018.05.041

17. M. Zeng, Y. Li, Recent advances in heterogeneous electrocatalysts for the hydrogen evolution reaction. J. Mater. Chem. A. **3**(29), 14942–14962 (2015). https://doi.org/10.1039/c5ta02974k

18. A. Pozio, F. Bozza, G. Nigliaccio, M. Platter, G. Monteleone, Development perspectives on low-temperature electrolysis. Energ. Ambiente Innov. **1**, 66–72 (2021). https://doi.org/10.12910/EAI2021-014

19. Y.H. Li, P.F. Liu, L.F. Pan, H.F. Wang, Z.Z. Yang, L.R. Zheng et al., Local atomic structure modulations activate metal oxide as electrocatalyst for hydrogen evolution in acidic water. Nat. Commun. **6**, 8064 (2015). https://doi.org/10.1038/ncomms9064

20. T.Y. Ma, S. Dai, M. Jaroniec, S.Z. Qiao, Metal-organic framework derived hybrid Co3O4-carbon porous nanowire arrays as reversible oxygen evolution electrodes. J. Am. Chem. Soc. **136**(39), 13925–13931 (2014). https://doi.org/10.1021/ja5082553

21. Z. Zhang, J. Liu, J. Gu, L. Su, L. Cheng, An overview of metal oxide materials as electrocatalysts and supports for polymer electrolyte fuel cells. Energy Environ. Sci. **7**(8), 2535–2558 (2014). https://doi.org/10.1039/c3ee43886d

22. F. Godínez-Salomón, L. Albiter, S.M. Alia, B.S. Pivovar, L.E. Camacho-Forero, P.B. Balbuena et al., Self-supported hydrous iridium–nickel oxide two-dimensional nanoframes for high activity oxygen evolution electrocatalysts. ACS Catal. **8**(11), 10498–10520 (2018). https://doi.org/10.1021/acscatal.8b02171

23. W. Zhou, J. Jia, J. Lu, L. Yang, D. Hou, G. Li, S. Chen et al., Recent developments of carbon-based electrocatalysts for hydrogen evolution reaction. Nano Energy **28**, 29–43 (2016). https://doi.org/10.1016/j.nanoen.2016.08.027

24. J. Zheng, Y. Zhang, X. Jing, X. Liu, T. Hu, T. Lv et al., Synthesis of amorphous carbon coated on V2O3 core-shell composites for enhancing the electrochemical properties of V2O3 as supercapacitor electrode. Colloids. Surf. A. **518**, 188–196 (2017). https://doi.org/10.1016/j.colsurfa.2017.01.035

25. N. Kaur, R.A. Mir, O.P. Pandey, Electrochemical and optical studies of facile synthesized molybdenum disulphide (MoS2) nano structures. J. Alloy. Compd. **782**, 119–131 (2019). https://doi.org/10.1016/j.jallcom.2018.12.145

26. N. Hassan, J. Riaz, M.T. Qureshi, A. Razaq, M. Rahim, A.M. Toufiq et al., Vanadium oxide (V2O3) for energy storage applications through hydrothermal route. J. Mater. Sci.: Mater. Electron. **29**(18), 16021–16026 (2018). https://doi.org/10.1007/s10854-018-9689-5

27. R.A. Mir, O.P. Pandey, Waste plastic derived carbon supported Mo2C composite catalysts for hydrogen production and energy storage applications. J. Clean. Prod. **218**, 644–655 (2019). https://doi.org/10.1016/j.jclepro.2019.02.004

28. K. Rajrana, A. Gupta, R.A. Mir, O.P. Pandey, Facile sono-chemical synthesis of nanocrystalline MnO2 for catalytic and capacitive

applications. Physica B **564**, 179–185 (2019). https://doi.org/10.1016/j.physb.2019.04.002

29. A. Varghese, S. D. KR, D. Pinheiro, & M. K. Mohan. Molecular architecture of PANI/V2O5/MnO2 composite designed for hydrogen evolution reaction. Surfaces and Interfaces, **41**, 103221 (2023). https://doi.org/10.1016/j.surfin.2023.103221

30. J. Zhang, H. Zhang, M. Liu, Q. Xu, H. Jiang, & C. Li. Cobalt-stabilized oxygen vacancy of V2O5 nanosheet arrays with delocalized valence electron for alkaline water splitting. Chem. Eng. Sci. **227**, 115915 (2020). https://doi.org/10.1016/j.ces.2020.115915

31. Q. Zhang, Z.L. Zhe Ru, R. Daiyan, P. Kumar, J. Pan, X. Lu et al., Surface reconstruction enabled efficient hydrogen generation on a cobalt-iron phosphate electrocatalyst in neutral water. ACS Appl. Mater. Interfaces **13**(45), 53798–53809 (2021). https://doi.org/10.1021/acsami.1c14588

32. Wang J, Zhang H, Wang X, Recent methods for the synthesis of noble-metal-free hydrogen-evolution electrocatalysts: from nanoscale to sub-nanoscale. Small Methods **1**(6) (2017). https://doi.org/10.1002/smtd.201700118.

33. K.K. Dey, S. Jha, A. Kumar, G. Gupta, A.K. Srivastava, P.P. Ingole et al., Layered vanadium oxide nanofibers as impressive electrocatalyst for hydrogen evolution reaction in acidic medium. Electrochimica Acta **312**, 89–99 (2019). https://doi.org/10.1016/j.electacta.2019.04.185

34. A. Badreldin, A. Abdel-Wahab, P.B. Balbuena, Local surface modulation activates metal oxide electrocatalyst for hydrogen evolution: synthesis, characterization, and DFT study of novel black ZnO. ACS Appl. Energy Mater. **3**(11), 10590–10599 (2020). https://doi.org/10.1021/acsaem.0c01642

35. J. Yang, X. Chen, X. Liu, Y. Cao, J. Huang, Y. Li et al., From Hexagonal to monoclinic: engineering crystalline phase to boost the intrinsic catalytic activity of tungsten oxides for the hydrogen evolution reaction. ACS Sustain. Chem. Eng. **9**(16), 5642–5650 (2021). https://doi.org/10.1021/acssuschemeng.1c00485

36. H. Qiao, X. Zhu, Z. Zheng, L. Liu, L. Zhang, Synthesis of V3O7·H2O nanobelts as cathode materials for lithium–ion batteries. Electrochem. Commun. **8**(1), 21–26 (2006). https://doi.org/10.1016/j.elecom.2005.10.021

37. N. Bahlawane, D. Lenoble, Vanadium oxide compounds:structure, properties, and growth from the gas phase. Chem. Vapor Depos. **20**(7-8–9), 299–311 (2014). https://doi.org/10.1002/cvde.201400057

38. J. Pan, M. Li, Y. Luo, H. Wu, L. Zhong, Q. Wang et al., Microwave-assisted hydrothermal synthesis of V2O5 nanorods assemblies with an improved Li-ion batteries performance. Mater. Res. Bull. **74**, 90–95 (2016). https://doi.org/10.1016/j.materresbull.2015.10.020

39. Y. Sun, Z. Xie, Y. Li, Enhanced lithium storage performance of V(2)O(5) with oxygen vacancy. RSC Adv. **8**(69), 39371–39376 (2018). https://doi.org/10.1039/c8ra07326k

40. He J, Liu F, Chen Y, Liu X, Zhang X, Zhao L, et al., Cathode electrochemically reconstructed V-doped CoO nanosheets for enhanced alkaline hydrogen evolution reaction. Chem. Eng. J. **432** (2022). https://doi.org/10.1016/j.cej.2021.134331.

41. X. Shang, J.-Q. Chi, S.-S. Lu, B. Dong, Z.-Z. Liu, K.-L. Yan et al., Hierarchically three-level Ni3(VO4)2@NiCo2O4 nanostructure based on nickel foam towards highly efficient alkaline hydrogen evolution. Electrochim. Acta **256**, 100–109 (2017). https://doi.org/10.1016/j.electacta.2017.10.017

42. X. Shang, J.-Q. Chi, Z.-Z. Liu, B. Dong, K.-L. Yan, W.-K. Gao et al., Ternary Ni-Fe-V sulfides bundles on nickel foam as free-standing hydrogen evolution electrodes in alkaline medium. Electrochim. Acta. **256**, 241–251 (2017). https://doi.org/10.1016/j.electacta.2017.10.050

43. Li Y, Tan X, Yang W, Bo X, Su Z, Zhao T, et al., Vanadium oxide clusters decorated metallic cobalt catalyst for active alkaline

44. hydrogen evolution. Cell Rep. Phys. Sci. **1**(12) (2020). https://doi.org/10.1016/j.xcrp.2020.100275

44. Y. Wang, Z. Zhang, Y. Zhu, Z. Li, R. Vajtai, L. Ci et al., Nanostructured VO2 Photocatalysts for hydrogen production. ACS Nano **2**(7), 1492–1496 (2008). https://doi.org/10.1021/nn800223s

45. S. Chalotra, R.A. Mir, G. Kaur, O.P. Pandey, Oxygen deficient V2O3: a stable and efficient electrocatalyst for HER and high performance EDLCs. Ceram. Int. **46**(1), 703–714 (2020). https://doi.org/10.1016/j.ceramint.2019.09.023

46. M. Rafique, M. Hamza, M. Shakil, M. Irshad, M.B. Tahir, M.R. Kabli, Highly efficient and visible light–driven nickel–doped vanadium oxide photocatalyst for degradation of Rhodamine B Dye. Appl. Nanosci. **10**, 2365–2374 (2020). https://doi.org/10.1007/s13204-020-01429-4

47. V.S. Vinila, J. Isac, Chapter 14 - Synthesis and structural studies of superconducting perovskite GdBa2Ca3Cu4O10.5+δ nanosystems. In *Design, fabrication, and characterization of multifunctional nanomaterials,* ed. by S. Thomas, N. Kalarikkal N, A. R. Abraham (Elsevier, 2022), pp. 319–341. https://doi.org/10.1016/B978-0-12-820558-7.00022-4

48. A.S. Hassanien, A.A. Akl, Effect of Se addition on optical and electrical properties of chalcogenide CdSSe thin films. Superlattices Microstruct. **89**, 153–169 (2016). https://doi.org/10.1016/j.spmi.2015.10.044

49. P. Makula, M. Pacia, W. Macyk, How to correctly determine the band gap energy of modified semiconductor photocatalysts based on UV-Vis spectra. J. Phys. Chem. Lett. **9**(23), 6814–6817 (2018). https://doi.org/10.1021/acs.jpclett.8b02892

50. A. Dal Corso, A. Pasquarello, A. Baldereschi, R. Car, Generalized-gradient approximations to density-functional theory: A comparative study for atoms and solids. Phys. Rev. B **53**(3), 1180 (1996). https://doi.org/10.1103/PhysRevB.53.1180

51. J.G. Lee, Computational materials science: an introduction, 2nd edn. (CRC Press, 2016). https://doi.org/10.1201/9781315368429.

52. D. Saraf, S. Chakraborty, A. Kshirsagar, R. Ahuja, In pursuit of bifunctional catalytic activity in PdS2 pseudo-monolayer through reaction coordinate mapping. Nano Energy **49**, 283–289 (2018). https://doi.org/10.1016/j.nanoen.2018.04.019

53. P. Hejduk, M. Szaleniec, M. Witko, Molecular and dissociative adsorption of water at low-index V2O5 surfaces: DFT studies using cluster surface models. J. Mol. Catal. A: Chem. **325**(1–2), 98–104 (2010). https://doi.org/10.1016/j.molcata.2010.04.004

54. Liu H, Zhang J-M, Effect of two identical 3d transition-metal atoms M doping (M = V, Cr, Mn, Fe, Co, and Ni) on the structural, electronic, and magnetic properties of ZnO. physica status solidi (b). **254**(10) (2017). https://doi.org/10.1002/pssb.201700098.

55. A. Badreldin, M.D. Imam, Y. Wubulikasimu, K. Elsaid, A.E. Abusrafa, P.B. Balbuena, A. Abdel-Wahab, Surface microenvironment engineering of black V2O5 nanostructures for visible light photodegradation of methylene blue. J. Alloys. Compds. **871** (2021). https://doi.org/10.1016/j.jallcom.2021.159615.

56. N.S. Kumar, J.H. Chang, M.-S. Ho, B. Balraj, S. Chandrasekar, B. Mohanbabu et al., Impact of Zn2+ doping on the structural, morphological and photodiode properties of V2O5 nanorods. J. Inorg. Organomet. Polym Mater. **31**(3), 1066–1078 (2020). https://doi.org/10.1007/s10904-020-01751-y

57. B.N. Reddy, B.M. Reddy, M. Subrahmanyam, Dispersion and 3-picoline ammoxidation investigation of V2O5/α-Al2O3 catalysts. J. Chem. Soc. Faraday Trans. **87**(10), 1649–55 (1991). https://doi.org/10.1039/FT9918701649

58. H. Nakao, K. Ohwada, N. Takesue, Y. Fujii, M. Isobe, Y. Ueda et al., Lattice dimerization and strain in inorganic spin-Peierls compound NaV2O5. Phys. B: Condensed Matter **241**, 534–536 (1997). https://doi.org/10.1016/S0921-4526(97)00636-4

59. A. Monshi, M.R. Foroughi, M.R. Monshi, Modified Scherrer equation to estimate more accurately nano-crystallite size using

XRD. World J. Nano Sci. Eng. **2**(3), 154–160 (2012). https://doi.org/10.4236/wjnse.2012.23020

60. A. Badreldin, A. Nabeeh, Z.K. Ghouri, J. Abed, N. Wang, Y. Wubulikasimu, K. Youssef, D. Kumar, M.K. Stodolny, K. Elsaid, E.H. Sargent, A. Abdel-Wahab, Early transition-metal-based binary oxide/nitride for efficient electrocatalytic hydrogen evolution from saline water in different pH environments. ACS Appl. Mater. Interfaces. **13**(45), 53702–16 (2021). https://doi.org/10.1021/acsami.1c13002

61. A. Badreldin, J. Abed, N. Hassan, A. El-Ghenymy, W. Suwaileh, Y. Wubulikasimu, Z.K. Ghouri, K. Youssef, D. Kumar, K. Elsaid, E.H. Sargent, A. Abdel-Wahab, Sulfide interlayered cobalt-based oxynitrides for efficient oxygen evolution reaction in neutral pH water and seawater. Appl. Catal. B **330**, 122599 (2023). https://doi.org/10.1016/j.apcatb.2023.122599

62. H.A. El-Sayed, A. Weiß, L.F. Olbrich, G.P. Putro, H.A. Gasteiger, OER catalyst stability investigation using RDE technique: a stability measure or an artifact? J. Electrochem. Soc. **166**(8), F458–F464 (2019). https://doi.org/10.1149/2.0301908jes

63. M. Vasilopoulou, A. Soultati, D.G. Georgiadou, T. Stergiopoulos, L.C. Palilis, S. Kennou et al., Hydrogenated under-stoichiometric tungsten oxide anode interlayers for efficient and stable organic photovoltaics. J Mater Chem A. **2**(6), 1738–1749 (2014). https://doi.org/10.1039/c3ta13975a

64. Rehman KU, Airam S, Lin X, Gao J, Guo Q, Zhang Z, In situ formation of surface-induced oxygen vacancies in Co(9)S(8)/CoO/NC as a bifunctional electrocatalyst for improved oxygen and hydrogen evolution reactions. Nanomaterials (Basel). **11**(9) (2021). https://doi.org/10.3390/nano11092237.

65. Y. Wang, L. Chen, X. Yu, Y. Wang, G. Zheng, Superb alkaline hydrogen evolution and simultaneous electricity generation by pt-decorated Ni3N nanosheets. Adv. Energy Mater. **7**(2), 1601390 (2017). https://doi.org/10.1002/aenm.201601390

66. E. Hryha, E. Rutqvist, L. Nyborg, Stoichiometric vanadium oxides studied by XPS. Surf. Interface Anal. **44**(8), 1022–1025 (2012). https://doi.org/10.1002/sia.3844

67. Hermann K, Chakrabarti A, Druzinic R, Witko M, Ab initio density functional theory studies of hydrogen adsorption at the V2O5(010) surface. physica status solidi (a). **173**(1):195–208 (1999). https://doi.org/10.1002/(SICI)1521-396X(199905)173:1<195::AID-PSSA195>3.0.CO;2-C.

68. H. Yao, Y. Chen, Y. Wei, Z. Zhao, Z. Liu, C. Xu, A periodic DFT study of ammonia adsorption on the V2O5 (001), V2O5 (010) and V2O5 (100) surfaces: Lewis versus Brönsted acid sites. Surf. Sci. **606**(21–22), 1739–1748 (2012). https://doi.org/10.1016/j.susc.2012.07.020

69. Li X, Sun Y, Ren F, Bai Y, Cheng Z, Smart oxygen vacancy engineering to enhance water oxidation efficiency by separating the different effects of bulk and surface vacancies. Mater. Today Energy. **19** (2021). https://doi.org/10.1016/j.mtener.2020.100619

70. A. Jovanović, A.S. Dobrota, L.D. Rafailović, S.V. Mentus, I.A. Pašti, B. Johansson, et al. Structural and electronic properties of V2O5 and their tuning by doping with 3d elements – modelling with DFT+U method and dispersion correction. Phys. Chem. Chem. Phys. 20,13934–43 (2018). https://doi.org/10.1039/C8CP00992A